

¹ **Ionospheric specification and space-weather forecasting with
2 an HF beacon network in the Peruvian sector**

D. L. Hysell¹, Y. Baumgarten², M. A. Milla³, A. Valdez³, and K. Kuyeng³

¹Earth and Atmospheric Sciences, Cornell

University, Ithaca, NY, USA

²Mechanical and Aerospace Engineering,

Cornell University, Ithaca, NY, USA

³Jicamarca Radio Observatory, Lima, Peru

3 Abstract. A network of HF transmitters and receivers used for ionospheric
4 specification is being installed in Peru. The HF transmitters employ multiple fre-
5 quencies and binary phase coding with pseudorandom noise (PRN), and the ob-
6 servables provided by the receivers include group delay, Doppler shift, ampli-
7 tude, bearing (from interferometry), and polarization. Statistical inverse meth-
8 ods are used to estimate *F*-region density in a volume from the data regionally.
9 The method incorporates raytracing based on the principles of Hamiltonian op-
10 tics in the forward model and involves an ionospheric parametrization in terms
11 of Chapman functions in the vertical and bicubic B-spline interpolation in the
12 horizontal. Regularization is employed to minimize the global curvature of the
13 reconstructions. HF beacon data for two nights in January, 2018, are presented.
14 We use the reconstructions to investigate why plasma irregularities associated
15 with equatorial spread *F* (ESF) formed on one occasion and not the other. The
16 data indicate that the background ionospheric flow is not simply frozen in, i.e.,
17 that longitude and local time variations cannot be equated, even at regional scales.
18 This has ramifications for ESF forecasting strategies which assume equivalence.

1. Introduction

19 The most important space weather agent at low geomagnetic latitudes is a class of convective
20 plasma instabilities operating in the postsunset *F*-region ionosphere. The instabilities produce
21 plasma density irregularities which cause range and frequency spreading in ionograms, a phe-
22 nomenon known as equatorial spread *F* (ESF) [*Booker and Wells, 1938*]. The irregularities also
23 cause diffraction and scattering in radio signals, posing a hazard to ground- and space-based
24 radio communication, navigation, and imaging systems (see *Woodman [2009]; Kelley et al.*
25 [2011] for recent reviews). In radar backscatter, the irregularities appear as spectacular plumes
26 ascending into the topside.

27 The dominant instabilities in ESF are variants of the collisional interchange instability which
28 occurs in plasmas where currents driven by gravity, a background electric field, and neutral
29 winds flow in regions where the Pedersen conductivity is finite and inhomogeneous such as the
30 postsunset bottomside *F* region [*Zargham and Seyler, 1987*]. By definition, inertia is negligible
31 in the collisional interchange instability which therefore does not produce inertial range turbu-
32 lence. Instead, instability tends to form steepened structures which occupy a broad continuum
33 of spatial scale sizes [*Costa and Kelley, 1978*]. The broadband aspect of the phenomenon makes
34 it disruptive to a wide range of systems.

35 The collisional interchange instability occurs frequently in the equatorial zone and is influ-
36 enced by but not dependent on solar and geomagnetic conditions. It has been studied analyt-
37 ically and with two- and three-dimensional numerical simulations for decades (e.g. *Ossakow*
38 [*1981*]; *Zargham and Seyler [1987]*; *Keskinen and Basu [1997]*; *Huba et al. [2008]*; *Retterer*
39 [*2010*]; *Yokoyama et al. [2014]*). While the most important characteristics observed experi-

40 mentally have been reproduced in simulation, the phenomenon has so far resisted numerical
41 forecasting.

42 A series of studies combining a 3D numerical simulation code with comprehensive iono-
43 spheric observations from the Jicamarca Radio Observatory has shown some forecasting
44 promise. [Hysell *et al.*, 2014a, b, 2015]. The simulation is initialized and forced so as to be
45 consistent with plasma density and drift profiles measured using the incoherent scatter tech-
46 nique at Jicamarca starting at sunset. Irregularities produced by the simulation can be compared
47 with those observed by Jicamarca using coherent-scatter techniques to assess forecast skill. A
48 novel feature of the simulation is that it encompasses vertical currents in the *F* region driven
49 by zonal winds. These currents are strong around sunset and can be the dominant driver for a
50 variant of collisional interchange instability [Hysell and Kudeki, 2004]. Another novel feature
51 of the simulation code is that it solves for the electrostatic potential fully in three dimensions.
52 This is necessary for recovering realistic flows and currents in the postsunset bottomside and
53 valley regions [Aveiro and Hysell, 2012].

54 The aforementioned simulation has not produced “false alarms” or predictions of irregulari-
55 ties that were not actually observed. It has produced some “missed detections,” failing to predict
56 some radar plumes and topside irregularities that were observed. A shortcoming of the forecast
57 strategy that could be responsible stems from the inability of the Jicamarca radar to observe
58 conditions other than those immediately overhead. The strategy extrapolates Jicamarca obser-
59 vations using a combination of empirical models and by equating local-time and longitudinal
60 variations in some model parameters. The approach appears to be limiting.

61 We have therefore expanded the experimental zone in latitude and longitude with the deploy-
62 ment of a regional network of HF beacons. Autonomous HF transmitters and receivers have

63 been deployed to four sites in Western Peru. CW signals are transmitted at two frequencies
64 using binary phase coding and PRN codes. Reception is performed with multiple antennas.
65 The observables are signal amplitude, group delay or pseudorange, Doppler shift or optical path
66 length, bearing (using interferometry), and polarization. Statistical inverse methods can be used
67 to estimate the ionospheric electron density regionally and to assess conditions leading to insta-
68 bility and ESF. The goal is to augment the ongoing ESF forecasting effort at Jicamarca using
69 ISR and beacon data captured together in campaigns.

70 Below, we describe the beacon network and the data processing, present some campaign data
71 taken in January of **2018**, and assess the possible contribution to ESF forecasting.

2. Beacon network

72 See Fig. 1 for a map of current and planned HF beacon station sites. The beacon network
73 presently consists of one transmitting station at Ancon ($11^{\circ}46'37''S$, $77^{\circ}09'1''W$, 51 masl), one
74 transmitting station at Ica ($14^{\circ}52'77''S$, $75^{\circ}44'08.02''W$, 402 masl), one receiving station at
75 Jicamarca with dual receivers ($11^{\circ}57'5.8''S$, $76^{\circ}52'27''W$, 510 masl), and one receiving station
76 in Huancayo with dual receivers ($12^{\circ}02'30''S$, $75^{\circ}19'15''W$, 3315 masl). While it is possible to
77 collocate transmitting and receiving stations, we have yet to do so.

78 Each beacon transmitter is actually two transmitters which deliver 0.5 W of continuous power
79 to two inverted-V antennas aligned northwest to southeast. The transmitters operate at 2.72 and
80 3.64 MHz. Each emits a unique pseud-random binary phase code (PRN) with a compression
81 ratio of 10,000. The code gain is subsequently increased to a factor of 1E6 in each Doppler bin
82 through coherent signal processing.

83 Each beacon receiver is a single receiver able to receive signals at two frequencies simul-
84 taneously. The receivers use broadband dipole antennas connected via low-noise amplifiers.

85 Two receivers are deployed at Huancayo and Jicamarca. At both sites, one receiving antenna is
 86 aligned northeast to southwest and the other northwest to southeast. The antennas are spatially
 87 offset, making it possible to measure both **polarization** and arrival angle (using interferometry).
 88 Receivers sample at a rate of 10 MS/s at an frequency intermediate between 2.72 and 3.64
 89 MHz. The output is then resampled at 1 MS/s. The effective sample rate is further reduced to
 90 100 kS/s through decimation, yielding a range resolution of 1.5 km. Each range gate is sampled
 91 every 100 ms and coherently processed for 10 s. The signal is then detected. Finally, spectra
 92 and cross spectra are incoherently integrated for 1 min.

PRN coding makes it possible to measure the group delay or pseudorange which is a measure of the time of flight of the signals. Formally, the pseudorange is defined as

$$\begin{aligned} L &\equiv \int \frac{c}{v_g} ds \\ &= \int \frac{d}{d\omega}(\omega n) ds \end{aligned}$$

where $n(\omega; k, \dots)$ is the real part of the index of refraction for the given propagating wave mode which is taken here to be positive, v_g is the group speed, c is the speed of light in vacuum, $\omega = 2\pi f$ is the angular frequency, and ds is an element along a ray path. The Doppler shift of the signal is meanwhile the negative of the time derivative of the optical path length which is defined as

$$l \equiv \int n ds$$

93 which is proportional to the physical length of the ray measured in wavelengths. By integrating
 94 the negative of the Doppler shift in time, it is possible to estimate the optical path length to
 95 within an additive constant.

It is illustrative to contrast the observables in an HF beacon experiment with comparable parameters derived from global positioning system (GPS) signals. Since L-band frequencies are much larger than any of the characteristic frequencies of ionospheric plasmas, the index of refraction can be approximated by the formula $n^2 \approx 1 - 80.48n_e/f^2$ where n_e is the electron number density such that n itself is always only slightly smaller than unity, viz. $n \sim 1 - \epsilon$ with ϵ proportional to n_e . In this limiting case, we can write

$$L \approx \int (1 + \epsilon) \, ds$$

$$l \approx \int (1 - \epsilon) \, ds$$

so that both the pseudorange and the optical path length deviate from the ray path length in proportion to the total electron density (TEC). The observables are essentially equivalent in terms of what they indicate about ionospheric structure. Measuring both is desirable in the context of GPS mainly because of differences in accuracy, precision, and bias.

In the case of HF beacon data, however, the index of refraction is a function of electron density, magnetic field intensity, magnetic aspect angle, electron-neutral collision frequency, and wave frequency given by the Booker quartic or the Appleton-Hartree equation (e.g. *Budden* [1985]):

$$n^2(\omega, \theta) = 1 - \frac{X}{1 - iZ - \frac{Y^2 \sin^2 \theta}{2(1-X-iZ)} \pm \sqrt{\frac{Y^4 \sin^4 \theta}{4(1-X-iZ)^2} + Y^2 \cos^2 \theta}} \quad (1)$$

(where $X \equiv \omega_p^2/\omega^2$, $Y \equiv \Omega/\omega$, and $Z \equiv \nu/\omega$, where the plus and minus signs correspond to the O and X modes, respectively, and where $\omega = 2\pi f$, ω_p , Ω , and ν are the wave, plasma, electron gyro, and electron-neutral collision frequencies, respectively. The angle θ is the angle between the wave vector and the background geomagnetic field.) The pseudorange and optical path length consequently represent very different moments of the ionospheric electron density.

¹⁰⁵ Measuring both independently is advantageous for ionospheric specification. Faraday rotation
¹⁰⁶ measurements could provide a third distinct moment in future experimental configurations.

¹⁰⁷ At each time step, the beacon data analysis algorithm determines the first range gate corre-
¹⁰⁸ sponding to the first-hop echo. This is interpreted as the pseudorange of the X-mode signal. The
¹⁰⁹ first moment of the Doppler spectrum in the given range gate is then interpreted as the Doppler
¹¹⁰ shift. Presently, only the X-mode pseudorange and the Doppler shift are utilized for analysis.

¹¹¹ In the future, it should also be possible to make use amplitude, arrival angle, and polarization,
¹¹² all quantities predicted during analysis, although that information is currently being neglected.

¹¹³ Likewise, only the first-hop signal is considered presently although data from multiple hops
¹¹⁴ could equally well be incorporated in the data inversion, albeit at increased computational cost
¹¹⁵ and with choices to be made regarding how ground reflection or scatter should be treated.

¹¹⁶ The pseudorange and Doppler shift for each of the transmitter-receiver links and each fre-
¹¹⁷ quency are used to estimate the ionospheric electron density in the vicinity of Jicamarca. The
¹¹⁸ inversion process involves three steps or loops. In the inner loop, rays are traced from a given
¹¹⁹ transmitting station using the equations of Hamiltonian optics which follow directly from Fer-
¹²⁰ mat's principle [Holm, 2011]. Our algorithm makes use of the formalism given by *Jones and*
¹²¹ *Stephenson* [1975]. We have implemented a high-order Adams multistep method to carry out
¹²² the raytracing [Shampine and Gordon, 1975]. The magnetic field used to compute the index
¹²³ of refraction is taken from the International Geomagnetic Reference Field [Thébault *et al.*,
¹²⁴ 2015]. The initial azimuth and elevation of the ray are specified, and the ray is traced through a
¹²⁵ parametrized ionosphere until it returns to the ground. In the middle loop, the azimuth and ele-
¹²⁶ vation are varied until the ray returns to the ground at the location of a given receiving station.

¹²⁷ This is effectively a shooting method for boundary value problems [Press *et al.*, 1988]. For each

128 ray, the pseudorange and the optical path length are calculated. The Doppler shift is calculated
129 from the negative of the time derivative of the latter. In practice, time derivatives are computed
130 using backwards differencing.

131 The outer loop involves updating the ionospheric parametrization to optimize the congruity
132 between the predicted and measured pseudorange and Doppler shift observables. The iono-
133 sphere is parametrized in the vertical as a three-parameter Chapman function and in the hor-
134 izontal as an expansion of bi-cubic B-splines [De-Boor, 1978]. The present parametrization
135 employs 15 B-spline coefficients in the zonal direction and 15 in the meridional direction. In
136 total, the regional ionosphere is parametrized using 675 coefficients. This figure is arbitrary.

137 Additional observables for the ionospheric reconstruction are derived from electron density
138 profiles measured by the Jicamarca incoherent scatter radar directly overhead. Discrepancies
139 between the measured and modeled profile at Jicamarca's latitude and longitude contribute to
140 the objective function used for reconstruction. In practice, initial guess for the ionospheric
141 reconstruction is horizontally homogeneous and nearly matches the initial ISR density profile.

142 Optimization is performed using a Levenberg Marquardt algorithm. Since the reconstruc-
143 tion problem is underdetermined, the algorithm is augmented with the inclusion of 2nd-order
144 Tikhonov regularization which minimizes the weighted sum of the global curvature of the model
145 ionosphere and the chi-squared parameter (see e.g. Hansen [2010]). Raytracing continues until
146 the model ionosphere is consistent with the available data. The current solution is used as the
147 initial guess for subsequent timesteps. Solutions are formed at 1-min. intervals. Additional
148 information about the algorithm and the underlying ionospheric model were given by Hysell
149 *et al.* [2016].

3. Jicamarca data

150 We examine campaign data from January 10 and 11, 2018. Ionospheric irregularities related
151 to ESF formed on the 10th but not on the 11th. Jicamarca observations for January 10 are
152 shown in Fig. 2. The top row of the figure shows, from left to right, electron density vs.
153 altitude and time, an electron density profile at 2400 UT, zonal plasma drifts vs. altitude and
154 time, and vertical plasma drifts vs. altitude and time. **(These parameters were estimated**
155 **using a specialized incoherent scatter mode at Jicamarca that measures vertical and zonal**
156 **plasma drifts, plasma number density, electron and ion temperature, and ion composition**
157 **simultaneously. The mode subdivides the main antenna array at Jicamarca into subarrays**
158 **and relies on time division multiplexing. The accuracy of the measurements is somewhat**
159 **compromised as a result.)** The bottom row shows a zonal plasma drift profile at 2400 UT in
160 the left panel. The right panel depicts coherent scatter from 3-m plasma density irregularities
161 which are telltale of instability. Coherent scatter is much stronger than and obscures incoherent
162 scatter, making plasma parameter estimation impossible in the affected altitudes and times.

163 The event in question is not a likely candidate for topside ESF. The zonal plasma drifts are
164 modest (uniformly less than about 50 m/s at 2400 UT) and suggestive of relatively weak zonal
165 thermospheric winds. The vertical plasma drifts are also modest, the prereversal enhancement
166 reaching no more than about 20 m/s at its peak at about 2430 UT. The main drivers of the
167 collisional interchange instability are therefore weak. The peak plasma density is also low (less
168 than $5 \times 10^{11} \text{ m}^{-3}$ at 2400 UT), a consequence of the 10.7 cm solar flux index being only about
169 70, and the *F* layer is neither elevated nor rising at the time when ESF is most likely to occur.
170 The bottomside *F* region density gradient is, however, relatively steep.

171 Nevertheless, the coherent scatter observations show that the *F* region became unstable and
172 produced intense plasma density irregularities, first in the valley region and then in the bot-
173 tomside. Eventually, several topside plumes were detected, reaching altitudes of about 500
174 km. This is a marginal example of topside ESF but one that could likely have interfered with
175 trans-ionospheric radio communications.

176 A more incisive view of the radar plumes observed on Jan. 10, 2018, is afforded by the appli-
177 cation of spaced-antenna methods and aperture-synthesis analysis to the coherent scatter data.
178 The techniques determines the spatial distribution of scatterers within the transmitter beam.
179 (For radar imaging purposes, a transmitting antenna module with a half-power full beamwidth
180 of about 6° degrees is employed.) Fig. 3 shows images of the earliest plume detected computed
181 at three times spanning the interval when the plume was contained within the radar beam. The
182 images show that the plume was developing rapidly during the time it traversed the radar beam.
183 Having barely emerged from a bottomside layer by about 2020 LT, the plume had penetrated
184 into the topside a mere 10 min. later. The morphology of the plume, which is typical of the
185 events observed in this way, can be used to validate the numerical simulations discussed in the
186 next section.

187 In contrast, Fig. 4 shows Jicamarca observations for Jan. 11, 2018, when no ESF irregularities
188 were observed. By comparison to the Jan. 10 event, this one is characterized by slightly denser
189 ionization at the *F*-region peak and by stronger zonal plasma drifts which also exhibit shear
190 flow in the bottomside more distinctly. The plasma density gradient in the bottomside *F* region
191 is shallower, however. Most importantly, there is almost no prereversal enhancement in the
192 vertical plasma drift which is slightly downward throughout the postsunset period. The Jan. 11
193 event is superficially therefore even less auspicious for topside ESF than the Jan. 10 event.

194 The coherent scatter observations show that no irregularities were produced on Jan. 11. The
195 complete absence of postsunset F -region irregularities is unusual at all solar flux levels and in
196 all seasons except June solstice at Jicamarca [Fejer *et al.*, 1999]. The Jan. 10 and Jan. 11
197 datasets, which were produced under comparable solar and geomagnetic conditions, therefore
198 provide a clear contrast that invites further study.

4. Numerical simulations

199 The likelihood of occurrence of ESF can be examined more quantitatively by simulating the
200 collisional interchange instability numerically. The simulation code we use is a fluid simulation
201 which solves for the electrostatic potential and ion composition in a three-dimensional volume
202 encompassing the equatorial ionosphere in the Peruvian sector. The horizontal neutral wind and
203 the background zonal electric field are specified continuously (together with gravity) as drivers
204 for the simulation. In the inertialess limit, the ion and electron momentum equations can be
205 solved explicitly. The simulation finds the potential by solving the quasineutrality condition
206 in a dipole magnetic coordinate system using a preconditioned stabilized biconjugate gradient
207 method with generalized mixed (Robin) boundary conditions. It then updates the number den-
208 sity of four ion species (O^+ , NO^+ , O_2^+ , and H^+) plus electrons by solving the continuity equa-
209 tion for each species. Charge exchange and dissociative recombination chemistry is included
210 although photo production is not in our postsunset model.

211 A flux-assignment scheme based on the the total variation diminishing condition (TVD) is
212 used to evaluate the convective derivative in the ion continuity equation [Harten, 1983; Trac
213 and Pen, 2003]. We use a second order TVD scheme with flux limiting (e.g. Van-Leer [1974])
214 formulated as a MUSCL (monotone upwind schemes for conservation laws). The approach
215 minimizes diffusion and dispersion in the time advance. The method is extended to 3D using a

216 dimensional splitting technique [Strang, 1968]. Time advance is via a 2nd order Runge-Kutta
 217 scheme. Neutral atmospheric parameters are imported from the NRLMSISE-00 model [Picone
 218 *et al.*, 2002]. The initial ion composition is taken from the IRI-2007 model [Bilitza and Reinisch,
 219 2008]. More detailed descriptions of the numerical methods involved were given by Hysell *et al.*
 220 [2014a, b, 2015].

221 The initial 3D plasma number density is interpolated from a run of the SAMI2 model which
 222 computes ionospheric state parameters as functions of altitude, latitude, and local time [Huba
 223 *et al.*, 2000]. For interpolation, we equate local time with longitude here. The solar flux and
 224 background electric field parameters used in SAMI2 are scaled to achieve the best overall con-
 225 gruence with electron density profiles measured over Jicamarca at a specified time which will
 226 be the start time of the simulation.

227 Subsequently, forcing is imposed on the simulation through horizontal neutral winds and
 228 background zonal electric field specifications. We import winds from the horizontal wind model
 229 (HWM) [Drob *et al.*, 2015]. The winds are scaled to achieve the best congruity between mea-
 230 sured and predicted zonal plasma drifts at the start of the simulation. **We have found that the**
 231 **modeled plasma drifts resulting from the HWM winds are generally very similar to the**
 232 **measured zonal plasma drifts given scale factors close to unity.** To specify the background
 233 zonal electric field, we fit a simple functional model to the measured vertical drifts shown in
 234 Fig. 2. Longitude and local time are equated once again here.

235 Results of a simulation of the Jan. 10, 2018, event are shown in Fig. 5. The simulation was
 236 initialized at 2400 UT in the Peruvian sector. Throughout this simulation, both the horizontal
 237 neutral winds and the background zonal electric field are modest. Current density in the zonal
 238 and meridional planes consequently remains small compared to the other simulations we have

239 documented. The strongest currents in the equatorial plane are in the vertical direction and arise
240 from an inefficient *F* region dynamo and differential plasma and neutral horizontal motions.
241 A vortex is evident after 30 min. when bottom-type plasma density irregularities excited by
242 vertical currents can be seen to be forming at the base of the bottomside. After 90 min., normal
243 collisional interchange instability is underway, with bottomside irregularities predominating
244 between 300-400 km altitude. At these altitudes, currents due to gravity are still small, and
245 zonal Pedersen currents driven by the background electric field are also small. The bottomside
246 irregularities therefore have not developed into major plumes although one or two have just
247 managed to enter the topside. The resemblance between the simulated depletions and the images
248 in Fig. 3 is fairly close except for the crucial fact that the depletions in simulation never show
249 the kind of rapid development seen in the images. This is a case of missed detection.

250 Fig. 6 shows results for the Jan. 11 event. In this case, the horizontal neutral winds are
251 much stronger than in the Jan. 10 case, and the current densities are consequently stronger. The
252 shallow bottomside density profile means that conductivity is distributed over a broader range of
253 altitudes than on Jan. 10, and competing neutral-wind dynamos in different altitude strata drive
254 strong field aligned currents throughout the region. However, the westward background electric
255 field that exists throughout the simulation is highly stabilizing, and irregularities never form –
256 even in the valley region. The simulation therefore correctly predicts the complete absence of
257 irregularities, bottom-type, bottomside, or topside, on Jan. 11.

5. Beacon data

258 To investigate the missed detection, we turn to data from the HF beacon network for wider
259 regional specifications of the ionosphere during the two events in question. Fig. 7 shows pseu-
260 dorange data for four ray paths and two frequencies (i.e. eight rays total) for Jan. 10 and 11,

261 2018, from 1800–2100 LT. Only the first hop is considered in each case. Prior to 1800 LT,
262 absorption typically renders reception unreliable. Data between midnight and sunrise typically
263 look similar to the curves shown here only with the altitude trend being reversed in time.

264 The pseudorange measurements are generally increasing functions of time during the periods
265 in question, although some wavelike behavior is sometimes also evident, particularly late in the
266 Jan. 10 event when the measurements reach a plateau. Different ray paths exhibit wavelike
267 variations at different times. The Ica ray paths, which are the longest, are the most variable,
268 particularly the Ica-Huancayo paths. The pseudoranges increased more rapidly with time on
269 Jan. 10 than Jan. 11. While this is consistent with the ISR drifts data in Figs. 2 and 4, the
270 pseudorange is obviously a poor proxy for and should not be regarded as a measurement of
271 the proper vertical motion of the ionospheric medium (whereas incoherent scatter does measure
272 proper motion). Proper vertical motion in this case is evidently not even the dominant factor
273 in the time rate of change of the pseudorange which is influenced by changes due to chemistry
274 and advection. Similar remarks hold for the optical path length observable which is considered
275 below. For a detailed investigation of the factors that control the Doppler shift of HF signals,
276 see *Bennett* [1972]. For clear examples of the distinction between HF Doppler measurements
277 and the proper motion of the ionosphere, see *Woodman et al.* [2006].

278 The difference between the pseudorange and the optical ray path is illustrated by Fig. 8.
279 In some cases, the two observables are similar. In this example, however, the two curves are
280 quite dissimilar in their details, even exhibiting different signs at times. Still greater differences
281 exist in some cases. We point this out just to highlight the fact that the two observables give
282 independent information about the ionosphere.

283 Ionospheric reconstructions based on HF beacon and Jicamarca ISR data are shown in Figs. 9
284 and 10 for Jan. 10 and 11, 2018, respectively. The figures have six panels, each representing
285 six different local times. (Recall that reconstructions are computed at a cadence of once per
286 minute.) Each panel shows two rays for two frequencies bridging the four transmitter-receiver
287 permutations possible in the network. Also shown is a parametrized electron density profile at
288 the latitude and longitude of Jicamarca. Isodensity contours for $N_e = 5 \times 10^{10} \text{ m}^{-3}$ (green) and
289 $3.5 \times 10^{11} \text{ m}^{-3}$ (cyan) are superimposed. Note that the isodensity contour heights are scaled to
290 emphasize horizontal gradients.

291 At 1800 LT, the data were consistent with a horizontally-uniform ionosphere. The HF rays
292 propagated along great-circle paths, and the ray pairs were each coplanar. Between 1800–1900
293 LT, the bottomside steepened under the influence of chemical recombination. Steepening pro-
294 ceeded from east to west with the motion of the solar terminator. The steep bottomside caused
295 the pseudoranges for the ray pairs to be similar despite the HF frequencies being different. By
296 1900 LT, the ionosphere was again nearly level and uniform across the region.

297 Between 1900–2000 LT, the ionosphere ascended in an action that also swept from east to
298 west with time. The zonal gradient in layer height was most evident at about 1930 LT. The gra-
299 dient was accompanied by HF rays propagating outside great-circle paths and by non-coplanar
300 ray pairs. By 2000 LT, the western edge had caught up with the eastern edge, and the ionosphere
301 was again nearly level. The event coincided with the passage of the prereversal enhancement
302 of the zonal electric field, a phenomenon the beacon technique is evidently able to track. Mon-
303 itoring the prereversal enhancement is critical for ESF forecasting. The HF network may be
304 superior to ISR measurements at Jicamarca in some respects, being more resilient to contami-
305 nation from plasma density irregularities.

306 After 2000 LT, however, the western edge of the region resumed its ascent, leading to the tilt in
307 the layer height evident in the reconstruction at 2020 LT. The tilt is significant since it indicates a
308 break in the equivalence of longitude with local time in the background flow. More specifically,
309 it indicates that the postsunset uplift was stronger to the west of Jicamarca's longitude than it
310 was directly overhead. In the reconstruction, the uplift sweeps from west to east, the eastern
311 edge of the region ultimately resising at a higher altitude than the western edge bt 2100 LT. As
312 the first radar plume of the evening was emerging at precisely 2020 LT, care must be taken with
313 the interpretation of the reconstructions at later times when changes in layer height are probably
314 better interpreted as effects rather than causes of instability and ionospheric irregularities.

315 In addition to the aforementioned secular variations, the ionospheric reconstruction also ex-
316 hibits wavelike and transient variations, although this is not apparent in the fixed frames in
317 Fig. 9. These seem to be much less important than the dramatic changes in layer height de-
318 scribed above however.

319 The Jan. 11, 2018, ionospheric reconstruction begins much the same way as the Jan. 10 event.
320 Between 1801 – 1900 LT, the bottomside steepens under the action of recombination in a manner
321 that progresses from east to west albeit to a lesser degree than on the previous evening. However,
322 there is little ionospheric evolution thereafter. Variations in layer height are small, gradual,
323 and uniform. There is no obvious prereversal enhancement. The most significant horizontal
324 gradients in layer height are meridional rather than zonal and may suggest the presence of
325 meridional winds which are generally (but not always) stabilizing [Huba and Krall, 2013].

6. Analysis

326 The original impetus for the beacon network were a few radar plumes seen over Jicamarca
327 in past campaigns when ionospheric conditions seemed unfavorable. The plumes in question

were seen mainly either immediately at sunset, when interchange instabilities should not have had sufficient time to produce well-developed radar plumes, or several hours after sunset, when the background electric field, neutral winds, and bottomside density gradient are typically unfavorable for instability. *Hysell et al.* [2015] speculated that external agents such as medium-scale traveling ionospheric disturbances (MSTIDs) or fossil plumes drifting in from the day side may have been responsible (see e.g. *Krall et al.* [2011]).

In the case of the Jan. 10, 2018, modest radar plumes were observed over Jicamarca in the time interval when plumes are most likely and under conditions that were unfavorable but not prohibitive for ESF, including a steep bottomside and a distinct if modest prereversal enhancement. The plumes developed to a greater degree than simulations based on Jicamarca ISR data anticipated, however. We turn to the HF beacon data to understand why.

Experimental results from individual ray paths on Jan. 10 and Jan. 11, 2018, as shown in Fig. 7, are suggestive. The pseudorange data suggest greater postsunset uplift on Jan. 10, something which was already obvious in the Jicamarca ISR data. They also suggest more irregular uplift from about 1930 LT onward when quasiperiodic fluctuations are evident in multiple traces. While it is tempting to associate the fluctuating drifts with gravity waves or other candidate ESF trigger agents, we note also that bottomside spread F irregularities were present by 1930 LT, and so the fluctuations could be indications of existing plasma waves and instabilities rather than of causes. It is also noteworthy that the fluctuations in the raw pseudorange data tend to diminish in the ionospheric reconstructions (e.g. Fig. 9). This is because small layer tilts generally give rise to large deviations in pseudorange as ray paths deviate from great-circle paths. Conversely, small tilts imply large pseudorange fluctuations. We should be reluctant to

350 read much into them, although small, wavelike fluctuations are visible in the full ionospheric
351 reconstructions when viewed completely in animated form (not shown).

352 The salient features of the Jan. 10 and 11, 2018, events are most apparent in the ionospheric
353 reconstructions (Figs. 9 and 10). Both reconstructions show the postsunset steepening of the
354 *F*-region bottomside. Only the Jan. 10 event shows steep zonal gradients in layer height. These
355 sweep through the field of view following the timing of the prereversal enhancement seen in the
356 Jicamarca ISR data through about 2000 LT. Crucially, however, the ionosphere on the west side
357 of the reconstruction reached higher altitude than the east side. Longer sustained vertical drifts
358 to the west of Jicamarca, as indicated by the HF beacon data, would have excited more devel-
359 oped interchange instabilities, irregularities, and depletions which would have drifted eastward
360 and over the observatory at a later time. This could explain how the radar plumes observed
361 on Jan. 10 developed. In this scenario, the background circulation defied the approximation
362 equating longitude and local time. A key assumption in the forecast methodology thus seems to
363 have been violated.

7. Summary

364 Previous after-the-fact forecast studies using the methodology and the simulation described
365 in this paper successfully reproduced the occurrence or non-occurrence of interchange insta-
366 bilities in the *F* region over Jicamarca during quiet geomagnetic conditions over a variety of
367 seasons and solar-flux levels [Hysell *et al.*, 2014a, b, 2015]. A few missed detections were also
368 documented, including radar plumes observed either too early or too late in the postsunset pe-
369 riod to be accounted for by the methodology or by conventional wisdom about the conditions
370 required for ESF. One possibility is that the radar plumes and underlying plasma density deple-
371 tions were generated under conditions that could not be captured by the Jicamarca ISR looking

372 immediately overhead. Such conditions could include exotic agents like thermospheric gravity
373 waves and MSTIDs or tamer factors such as a prereversal enhancement with a peak intensity
374 that varies with longitude.

375 In this study, small radar plumes were observed in the postsunset sector that were unremark-
376 able except for the fact that they were not anticipated by the numerical simulation. The back-
377 ground ionospheric conditions detected by the Jicamarca ISR did not seem very favorable for
378 the formation of topside plumes. The HF beacon data provided additional information about the
379 spatial configuration of the *F* region and the circulation, namely, that the amplitude of the pre-
380 reversal enhancement may have been larger to the west of Jicamarca than overhead. A change
381 of even a few m/s can be enough **to make** the difference between predicting bottomside spread
382 *F* and radar plumes.

383 The purpose of the HF beacon network is to expand the coverage of the Jicamarca Radio Ob-
384 servatory and offer a view into the horizontal structure of the regional ionosphere. Although the
385 network is still sparse, the eight paths between the four existing stations give indications about
386 east-west and north-south gradients at different altitudes. The group delay and Doppler shift
387 observables are uniquely informative, being sensitive to different aspects of the configuration
388 of the ionosphere. In the future, it should be possible to expand the network and to measure
389 and utilize other observables for reconstruction, including the arrival angle and the amplitude.
390 Modeling the absorption in particular could provide a view into the equatorial *D* region which
391 has so far been difficult to probe at Jicamarca. Incorporating data from multiple hops should be
392 possible if computationally expensive. Expanding the HF network in the north-south direction
393 would also provide a view into the strength of the meridional winds and the development of the
394 midlatitude anomalies, critical factors for ESF forecasting.

395 **Acknowledgments.** This work was supported by award FA9550-12-1-0462 from the Air
 396 Force Office of Scientific Research to Cornell University. The Jicamarca Radio Observatory
 397 is a facility of the Instituto Geofísico del Perú operated with support from NSF award AGS-
 398 1732209 through Cornell. The help of the staff is much appreciated. We also appreciate help
 399 with the SAMI2 model received from Dr. Joseph Huba at the Naval Research Laboratory. Data
 400 used for this publication are available through the Madrigal database.

References

401 Aveiro, H. C., and D. L. Hysell, Implications of the equipotential field line approximation for
 402 equatorial spread *F* analysis, *Geophys. Res. Lett.*, 39, doi: 10.1029/2012GL051,971, 2012.

403 Bennett, J. A., The ray theory of Doppler frequency shifts, *Aust. J. Phys.*, 21, 259, 1972.

404 Bilitza, D., and B. W. Reinisch, International Reference Ionosphere 2007: Improvements and
 405 new parameters, *Adv. Space Res.*, 42, 599–609, 2008.

406 Booker, H. G., and H. W. Wells, Scattering of radio waves by the *F* region., *Terres. Magn.*, 43,
 407 249, 1938.

408 Budden, K. G., *The Propagation of Radio Waves*, Cambridge Univ. Press, New York, 1985.

409 Costa, E., and M. C. Kelley, On the role of steepened structures and drift waves in equatorial
 410 spread *F*, *J. Geophys. Res.*, 83, 4359, 1978.

411 De-Boor, C., *A Practical Guide to Splines*, Springer Verlag, New York, 1978.

412 Drob, D. P., et al., An update to the Horizontal Wind Model (HWM): The quiet time thermo-
 413 sphere, *Earth and Space Science*, 2, doi:10.1002/2014EA000,089, 2015.

414 Fejer, B. G., L. Scherliess, and E. R. de Paula, Effects of the vertical plasma drift velocity on
 415 the generation and evolution of equatorial spread *F*, *J. Geophys. Res.*, 104, 19,859, 1999.

⁴¹⁶ Hansen, P. C., *Discrete Inverse Problems: Insight and Algorithms*, Siam, Philadelphia, 2010.

⁴¹⁷ Harten, A., High resolution schemes for hyperbolic conservation laws, *J. Com. Phys.*, **49**, 357,

⁴¹⁸ 1983.

⁴¹⁹ Holm, D. D., *Geometric Mechanics Part 1: Dynamics and Symmetry*, Imperial College Press,

⁴²⁰ London, 2011.

⁴²¹ Huba, J. D., and J. Krall, Impact of meridional winds on equatorial spread *F*: Revisited, *Geo-*

⁴²² *phys. Res. Lett.*, **40**, 1268–1272, doi:10.1002/grl.50,292, 2013.

⁴²³ Huba, J. D., G. Joyce, and J. A. Fedder, Sami2 is another model of the ionosphere (SAMI2): A

⁴²⁴ new low-latitude ionospheric model, *J. Geophys. Res.*, **105**, 23,035–23,054, 2000.

⁴²⁵ Huba, J. D., G. Joyce, and J. Krall, Three-dimensional equatorial spread *F* modeling, *Geophys.*

⁴²⁶ *Res. Lett.*, **35**, L10102, doi:10.1029/2008GL033,509, 2008.

⁴²⁷ Hysell, D. L., and E. Kudeki, Collisional shear instability in the eqautorial *F* region ionosphere,

⁴²⁸ *J. Geophys. Res.*, **109**, (A11,301), 2004.

⁴²⁹ Hysell, D. L., R. Jafari, M. A. Milla, and J. W. Meriwether, Data-driven numerical simulations

⁴³⁰ of equatorial spread *F* in the Peruvian sector, *J. Geophys. Res.*, p. doi:10.1002/2014JA019889,

⁴³¹ 2014a.

⁴³² Hysell, D. L., M. A. Milla, L. Condori, and J. W. Meriwether, Data-driven numerical simulations

⁴³³ of equatorial spread *F* in the Peruvian sector:2 Autumnal equinox, *J. Geophys. Res.*, p. doi:

⁴³⁴ 10.1002/2014JA020345, 2014b.

⁴³⁵ Hysell, D. L., M. A. Milla, L. Condori, and J. Vierinen, Data-driven numerical simulations of

⁴³⁶ equatorial spread *F* in the Peruvian sector 3: Solstice, *J. Geophys. Res.*, **120**, 10,809–10,822,

⁴³⁷ doi:10.1002/2015JA021,877, 2015.

438 Hysell, D. L., M. A. Milla, and J. Vierinen, A multistatic HF beacon network for ionospheric
 439 specification in the Peruvian sector, *Radio Sci.*, 51, doi:10.1002/2016RS005,951, 2016.

440 Jones, R. M., and J. J. Stephenson, A versatile three-dimensional ray tracing computer program
 441 for radio waves in the ionosphere, *Tech. Rep.* 75-76, U. S. Department of Commerce, 1975.

442 Kelley, M. C., J. J. Makela, O. de la Beaujardiere, and J. Retterer, Convective ionospheric
 443 storms: A review, *Rev. Geophys.*, 49, doi:10.1029/2010RG000,340, 2011.

444 Keskinen, M. J., and S. Basu, Nonlinear dynamics, bifurcation, and structure of high altitude
 445 equatorial ionospheric plasma bubbles, *J. Geophys. Res.*, 1997.

446 Krall, J., J. D. Huba, S. L. Ossakow, G. Joyce, J. J. Makela, E. S. Miller, and M. C. Kelley,
 447 Modeling of equatorial plasma bubbles triggered by non equatorial traveling ionospheric dis-
 448 turbances, *Geophys. Res. Lett.*, 38, doi:10.1029/2011GL046,890, 2011.

449 Ossakow, S. L., Spread *F* theories – A review, *J. Atmos. Terr. Phys.*, 43, 437, 1981.

450 Picone, J. M., A. E. Hedin, D. P. Drob, and A. C. Aikin, NRLMSISE-00 empirical model of
 451 the atmosphere: Statistical comparisons and scientific issues, *J. Geophys. Res.*, 107, A12, doi:
 452 10.1029/2002JA009,430, 2002.

453 Press, W. H., B. P. Flannery, S. A. Teukolsky, and W. T. Vetterling, *Numerical Recipes in C*,
 454 Cambridge Univ. Press, New York, 1988.

455 Retterer, J. M., Forecasting low-latitude radio scintillation with 3-D ionospheric plume models:
 456 1. Plume model, *J. Geophys. Res.*, 115, A03306, doi:10.1029/2008JA013,839, 2010.

457 Shampine, L. F., and M. K. Gordon, *Computer solution of ordinary differential equations, The*
 458 *initial value problem*, Freeman and Co., San Francisco, 1975.

459 Strang, G., On the construction and comparison of difference schemes, *SIAM J. Num. Anal.*, 5,
 460 506–517, 1968.

461 Thébault, E., et al., International geomagnetic reference field: the 12th generation, *Earth,*
462 *Planets, and Space*, 67, DOI: 10.1186/s40623-015-0228-9, 2015.

463 Trac, H., and U. L. Pen, A primer on Eulerian computational fluid dynamics for astrophysicists,
464 *Astrophysics*, 115, 303–321, 2003.

465 Van-Leer, B., Towards the ultimate conservation difference scheme. II. Monotonicity and con-
466 servation combined in a second-order scheme, *J. Comp. Phys.*, 14, 361, 1974.

467 Woodman, R. F., Spread F- An old equatorial aeronomy problem finally resolved?, *Ann. Geo-*
468 *phys.*, 27, 1915–1934, 2009.

469 Woodman, R. F., J. L. Chau, and R. R. Ilma, Comparison of ionosonde and inco-
470 herent scatter drift measurements at the magnetic equator, *Geophys. Res. Lett.*, 33,
471 doi:10.1029/2005GL023,692, 2006.

472 Yokoyama, T., H. Shinagawa, and H. Jin, Nonlinear growth, bifurcation and pinching of equa-
473 torial plasma bubble simulated by three-dimensional high-resolution bubble model, 119,
474 10,474–10,482, 2014.

475 Zargham, S., and C. E. Seyler, Collisional interchange instability, 1, Numerical simulations of
476 intermediate-scale irregularities, *J. Geophys. Res.*, 92, 10,073, 1987.

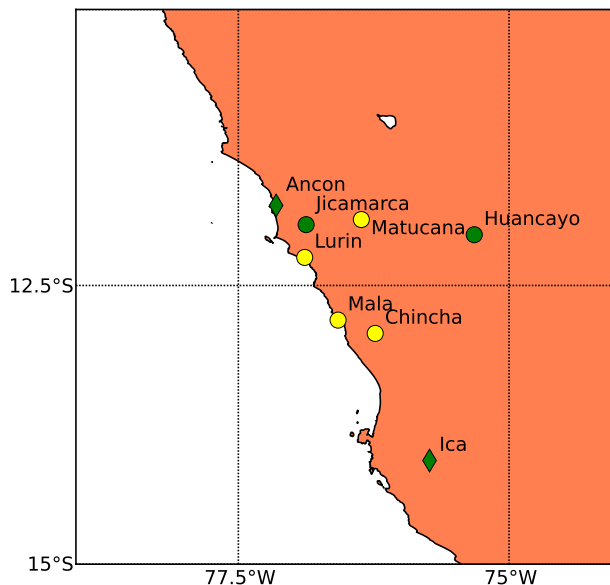


Figure 1. Map of current (green) and planned (yellow) HF beacon sites. Diamonds are transmit-only sites.

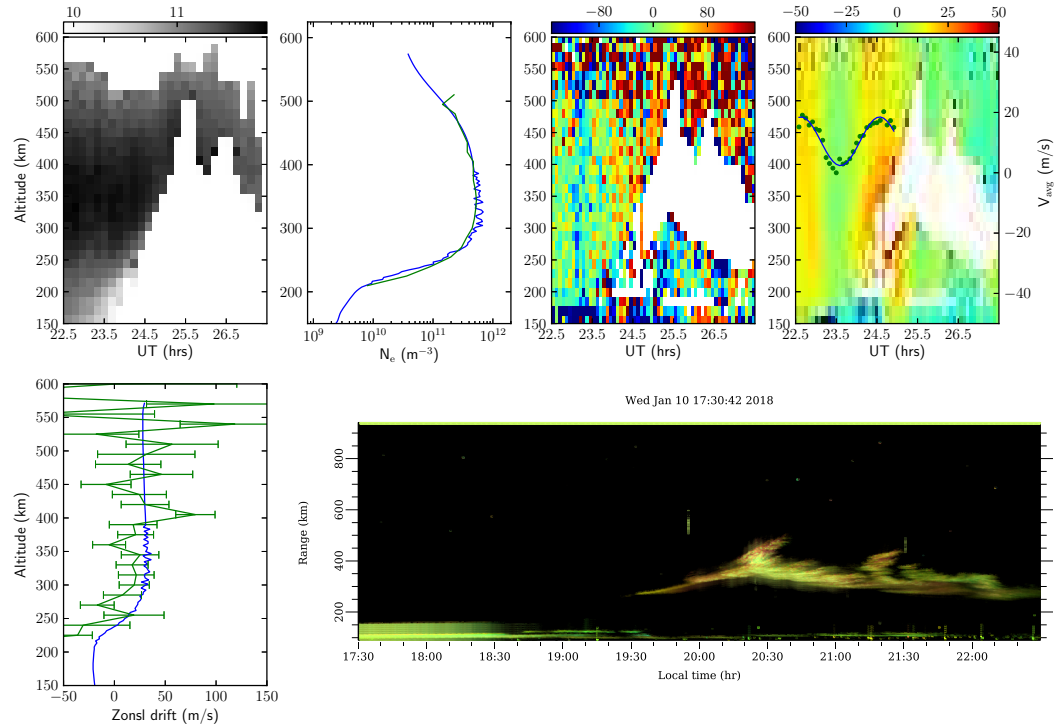


Figure 2. Jicamarca observations for Jan 10, 2018. Top row, from left to right: electron density, electron density profiles at 2400 UT (green line) together with computed density profile (blue line), zonal plasma drifts, and vertical plasma drifts. Altitude-averaged vertical drifts are shown by green plotter symbols, with the blue curve representing a fit to the data. Bottom row left: Measured zonal plasma drift profiles at 2400 UT (green line with error bars) together with a computed drift profile (blue line). Bottom row right: coherent backscatter. Note that UT = LT + 5 hr.

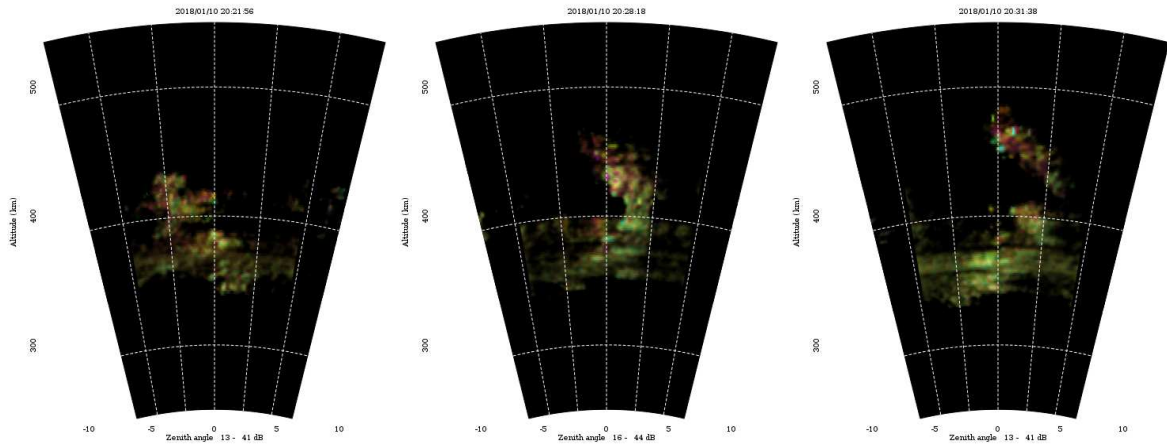


Figure 3. In-beam radar images of the first radar plume observed on Jan. 10, 2018. The images depict the backscatter as functions of range and bearing during short snapshots. The intensity, hue, and saturation of the image pixels convey information about the backscatter signal-to-noise ratio, Doppler shift, and spectral width, respectively. The images show the motion and evolution of the plume over a period of about 10 min.

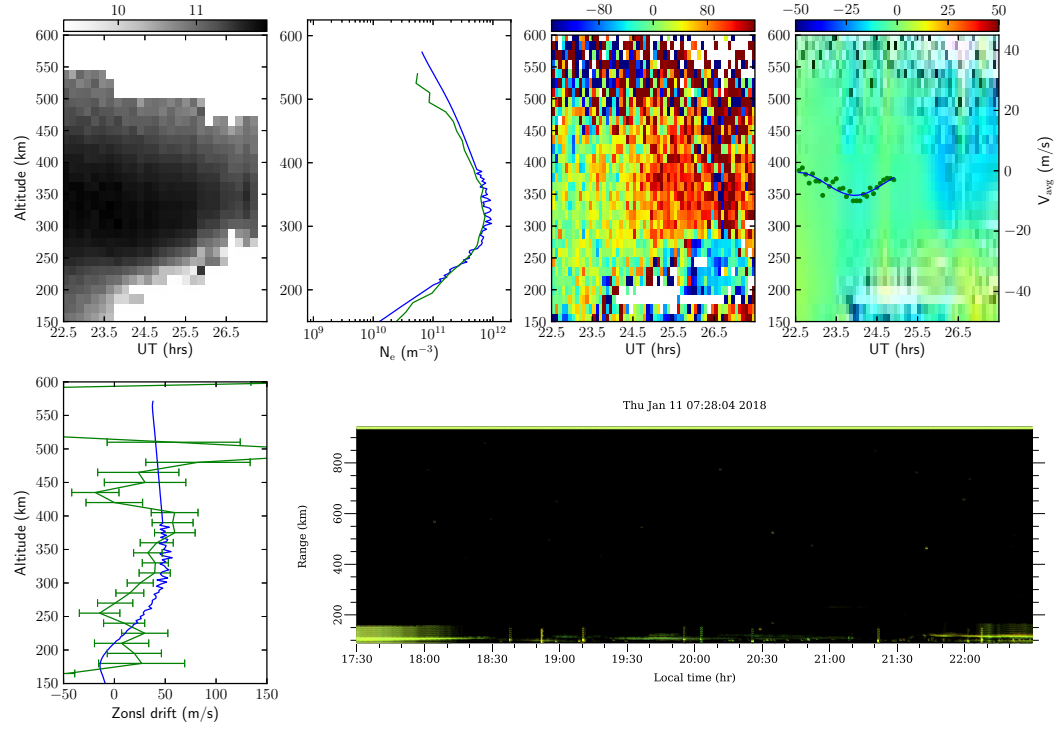


Figure 4. Same as Fig. 2 except for Jan 11, 2018. The plasma density and zonal drift profiles represent conditions at 2330 UT. Note that UT = LT + 5 hr.

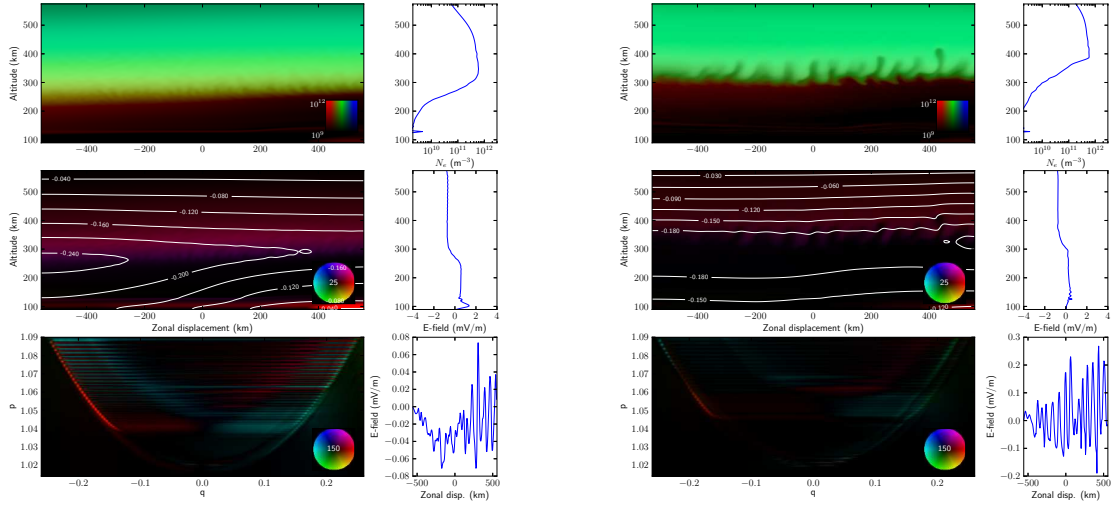


Figure 5. Numerical simulation of the Jan. 10, 2018, equatorial ionosphere over Jicamarca.

Figures at left and right depict conditions 30 and 90 min. after a simulation start time of 2400 UT, respectively. (top left panels) Ion number density. Red, green, and blue hues represent molecular ions, atomic ions, and hydrogen ions, respectively. (top right panels) Electron number density profiles through the geometric center of the simulation volume. (middle left panel) Current density in the equatorial plane with equipotentials superimposed. (middle right panel) Vertical electric field profile. (bottom left panels) Current density in the meridional plane. (bottom right panels) Zonal electric field along cut through geometric center of simulation.

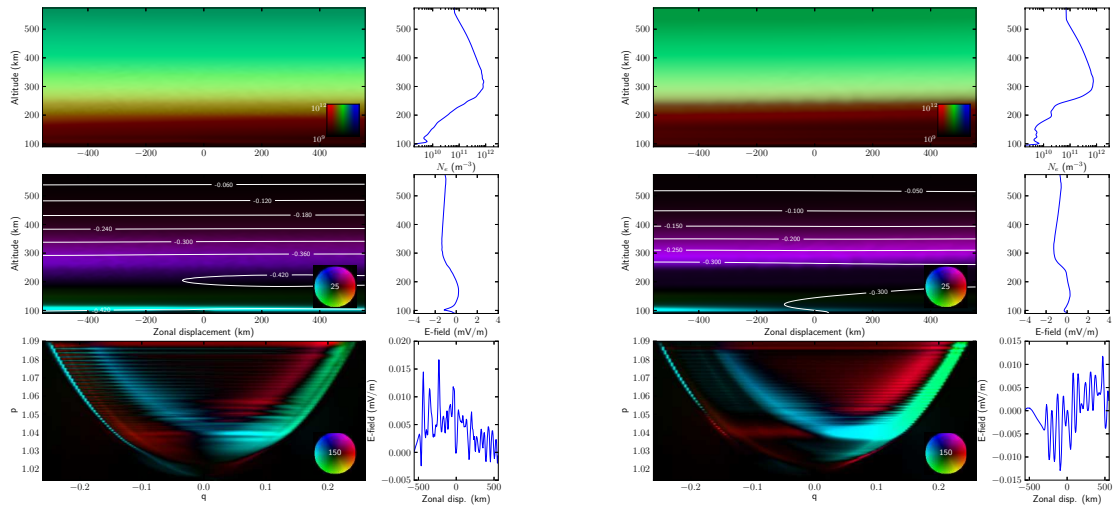


Figure 6. Numerical simulation of the Jan. 11, 2018, equatorial ionosphere over Jicamarca.

Figures at left and right depict conditions 30 and 90 min. after a simulation start time of 2330 UT, respectively.

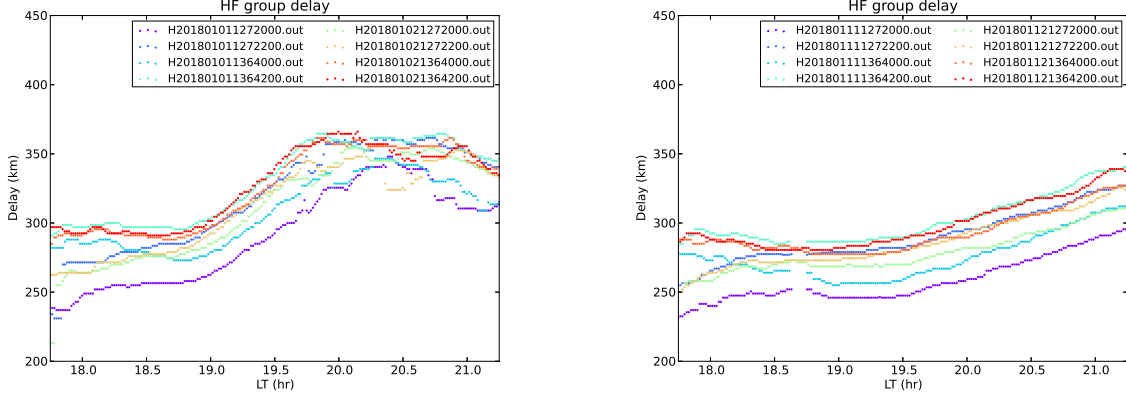


Figure 7. Pseudorange measurements for Jan. 10 (left) and Jan. 11 (right), 2018. The convention is to plot half the pseudorange, a quantity more closely comparable to altitude. Ray paths are designated by names of the form Hyyydddrrffft00.dat where yyyy is year, ddd is day number, rr is receiver, fff is frequency, and t is transmitter. The receiver options are 11 for Jicamarca and 21 for Huancayo. (We presently consider results for only one of the two receivers located at each site.) The transmitter options are 0 for Ancon and 2 for Ica.

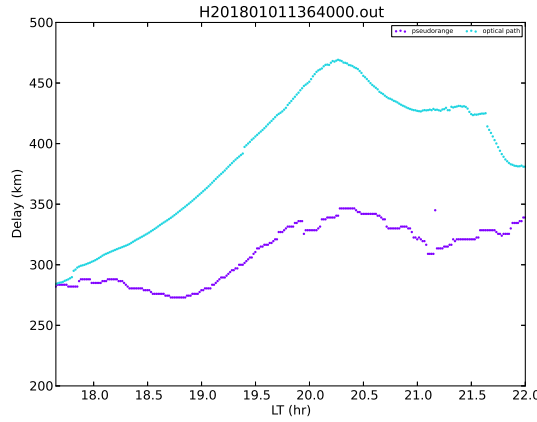


Figure 8. Comparison between pseudorange (violet) and optical path length (cyan) for the 3.64 MHz ray path between Ancon and Jicamarca on Jan. 10, 2018. The vertical offset of the optical ray path measurement, which is derived by integrating the negative of the Doppler shift, is arbitrary. By convention, both quantities were divided by two for plotting.

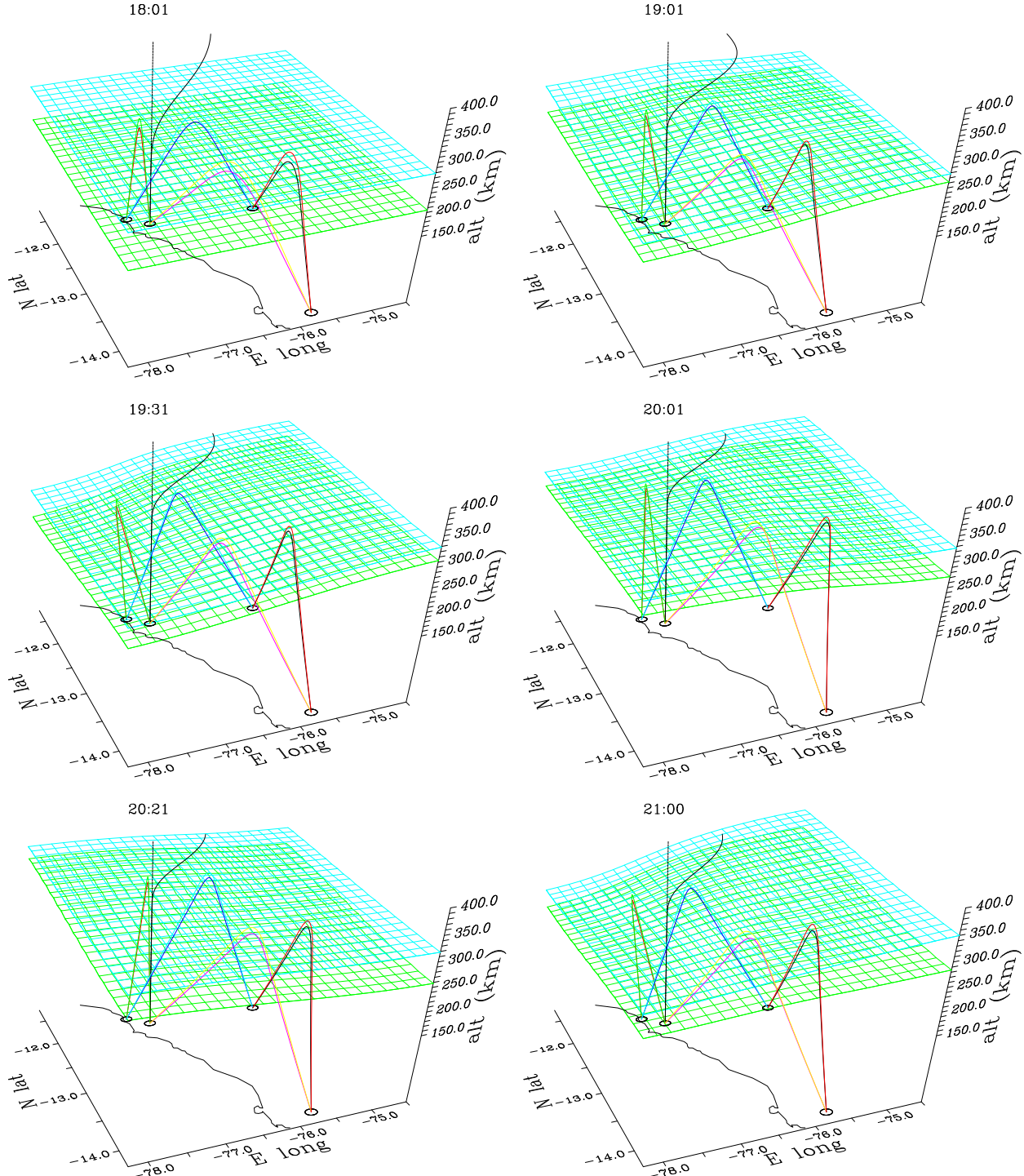


Figure 9. Ionospheric reconstruction for Jan. 10, 2018. Rays connect HF transmission and reception sites. A parametrized electron density profile is shown at the latitude and longitude of the Jicamarca Radio Observatory. Isodensity contours depict electron densities of $5 \times 10^{10} \text{ m}^{-3}$ (green) and $3.5 \times 10^{11} \text{ m}^{-3}$ (cyan). The curves are plotted so as to accentuate gradients, with departures from the mean contour height scaled by a factor of three.

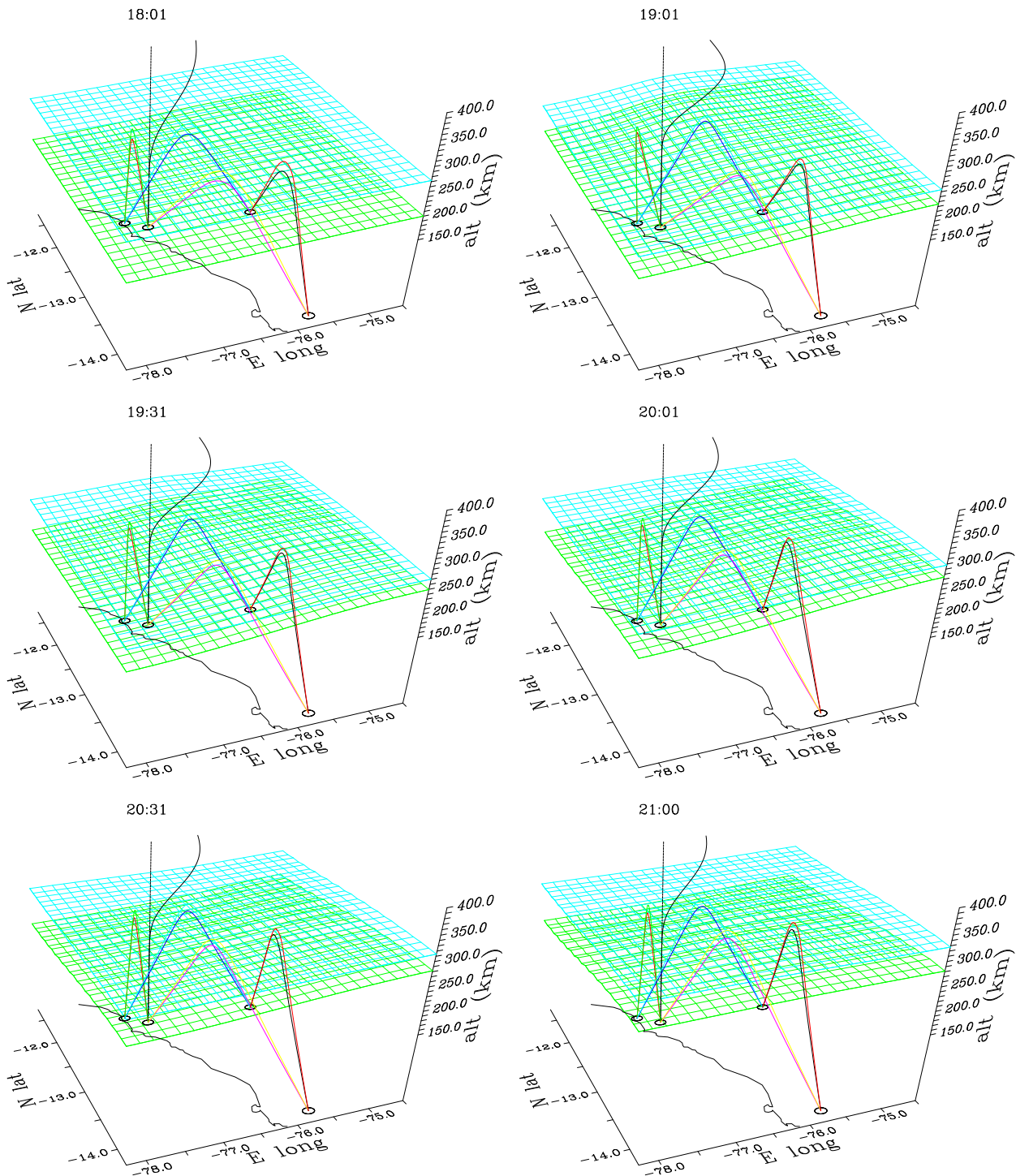


Figure 10. Ionospheric reconstruction for Jan. 11, 2018.